A global SS precursor method for imaging discontinuities: the Moho and beyond

Yuhang Dai[1], Saikiran Tharimena[1#], Catherine Rychert[1,2*], Nicholas Harmon[1,2]

[1] School of Ocean and Earth Science, University of Southampton, Southampton, UK

[2] Geology and Geophysics, Woods Hole Oceanographic Institution, Massachusetts, USA

[#] Currently at Schibsted ASA, Oslo, Norway

*Correspondence to: Catherine.Rychert@whoi.edu

Abstract

Imaging seismic velocity discontinuities within the Earth's crust and mantle offers important insight into our understanding of the tectonic plate, associated mantle dynamics, and the evolution of the planet. However, imaging velocity discontinuities in locations where station coverage is sparse, is sometimes challenging. Here we demonstrate the effectiveness of a new imaging approach using deconvolved SS precursor phases. We demonstrate its effectiveness by applying it to synthetic seismograms. We also apply it to ~1.6M SS precursor waveforms from the global seismic database (1990 – 2018) for comparison with Crust1.0. We migrate to depth and stack the data in circular 6° bins. The tests demonstrate that we can recover Moho depths as shallow as 20 km. The Moho is imaged at 21 – 67 km depth beneath continental regions. The Moho increases in depth from 21 km ± 4 km beneath the continental shelf to 45 – 50 km beneath the continental interiors and is as deep as 67 ± 4 km beneath Tibet. We resolve the Moho in 77 % of all continental bins, within 10 km of Crust 1.0, with all outliers located in coastal regions. We also demonstrate the feasibility of using this method to image discontinuities associated with the mantle transition zone with both synthetic and real data. Overall, the approach shows broad promise for imaging mantle discontinuities.

Keywords: Lithosphere, Body Waves, Asthenosphere, Crustal Imaging, Mantle discontinuities

1. Introduction

Earth's radial structure is characterized by distinct boundaries associated with variations in seismic velocity and density (Dziewonski & Anderson, 1981). Various physical and chemical processes are attributed to these variations. The shallowest of these boundaries include, for instance, the Moho, the lithosphere-asthenosphere boundary, and the transition zone

discontinuities. The Moho (Mohorovičić, 1910) defines a boundary between the chemically distinct and seismically slow crust from the faster mantle beneath. The lithosphere-asthenosphere boundary represents the transition from a rheologically strong and seismically fast lithosphere, comprised of the crust and a section of the upper mantle, to the deeper, weaker and seismically slower asthenosphere (Artemieva, 2011; Eaton et al., 2009; Fischer et al., 2010; Rychert et al., 2020; Rychert et al., 2018; Rychert & Shearer, 2009). The lithosphere is colder than the asthenosphere, and it may also be chemically distinct and/or partial melt may exist in the asthenosphere, further distinguishing the layers. The transition zone discontinuities are characterized by velocity increases with depth. They are typically interpreted as the pressure-induced solid-state transformation of olivine grains into denser crystal structures, or phase changes, predicted by laboratory experiments (Ringwood, 1975): α olivine to β-spinel (wadslyite) at ~410 km, β-spinel to ringwoodite at ~520 km and ringwoodite to silicate perovskite and magnesiowüstite at ~660 km (Ringwood, 1975).

Imaging seismic velocity discontinuities globally can help us better understand the tectonic plate, mantle convection, and the evolution of the planet (Bostock, 1999; Rychert et al., 2007; Rychert & Shearer, 2011; Shearer, 1991; Tharimena, Rychert, Harmon, et al., 2017); although, tight constraints on these discontinuities globally and self-consistently can be challenging. For example, both surface wave and body wave seismic tomography provide important constraints on the seismic velocity of the crust and the mantle (Harmon et al., 2009; Masters et al., 1996; Montagner & Tanimoto, 1991; Ritsema et al., 2011), but the models have more difficulty resolving the exact location and character of sharp seismic discontinuities (Rychert et al., 2005; Rychert et al., 2007). Receiver functions offer tighter constraints on the sharpness of velocity discontinuities but lack resolution in regions with sparse or no station coverage (Rychert et al., 2010). The highest resolution constraints come from active source studies, although these are limited in terms of spatial extent and also the depth to which they can image, with only very few studies imaging lithosphere-asthenosphere depths (Mehouachi & Singh, 2018; Roy Chowdhury, 2020; Stern et al., 2015).

SS phases are shear waves that have bounced once off the surface of the Earth roughly mid-way between the source and the receiver. SS precursors are underside reflections from

discontinuities that arrive just before the main SS phases, which are sensitive to the region of their bounce point (Figure 1a). These are referred to as SdS, where 'd' indicates the discontinuity of interest, for instance, SmS would refer to the SS reflection from the Moho. The advantage of these phases is that they offer resolution in locations where station coverage is sparse. However, SS waveforms and their precursors are relatively long-period waveforms. Precursors reflected from shallow discontinuities like the Moho and the lithosphere-asthenosphere boundary typically interfere with the surface-reflected SS waveforms, making them difficult to distinguish. Therefore, SS precursors have mostly been used to image deeper discontinuities such as the transition zone discontinuities (Flanagan & Shearer, 1998; Frazer & Park, 2023; Houser et al., 2008; Huang et al., 2019). To minimize waveform interference Schmerr (2012) considered acceleration seismograms, which are effectively filtered to higher frequencies and carefully selected data. The waveforms were stacked in bins and a discontinuity was detected approximately at lithosphere-asthenosphere depths (40 – 75 km) intermittently across the Pacific. In another approach Heit et al. (2010) deconvolved the SS waveform from itself before migrating and stacking in bins, imaging a discontinuity related to the Moho and the lithosphere-asthenosphere boundary beneath Asia. Rychert and Shearer (2010) developed a strategy to image discontinuities using SS-precursors by performing waveform modeling on the sidelobes of the stacked SS-waveforms. Synthetic waveforms were calculated by convolving a reference SS stack with impulse operators corresponding to a variety of discontinuity depths and characters, and the best-fitting discontinuity was determined via a grid search approach. They validated the method at shallow Moho depths by demonstrating agreement with the Crust2.0 (Bassin et al., 2000) and Mixture Density Network (MDN) (Meier et al., 2007) models in bins across Asia and extended the method to image the lithosphere-asthenosphere boundary across the Pacific using an attenuated S-wave as the reference waveform (Rychert & Shearer, 2010). Tharimena, Rychert, Harmon, et al. (2017) followed a similar procedure as Rychert and Shearer (2011) to image lithosphere-asthenosphere structure beneath the Pacific but implemented a differential evolution algorithm (Price et al., 2005; Storn & Price, 1997) to minimize both the model storage size and computation time in comparison to a typical grid search. The inclusion of 7 additional years of data (1990 – 2014 instead of 1990 -

2007) yielded a three-fold increase in the number of waveforms and a higher resolution result in which greater numbers of parameters could be explored. The study found discontinuities consistent with Schmerr (2012) and Rychert and Shearer (2011) but also found evidence for locations where either two discontinuities exist in depth and/or lithosphere-asthenosphere boundary depths vary laterally within a Fresnel zone of the waveforms.

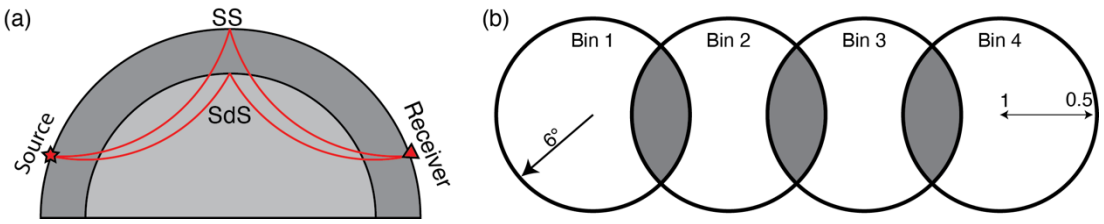

Figure 1: (a) Schematic showing ray paths of the SS and the SdS phases, which are sensitive to the structure beneath the bounce point, roughly halfway between the source and the receiver. SdS refers to the underside reflection of the S wave at a discontinuity, located at 'd' km depth, e.g. Moho, 410, 660. (b) Schematic representation of bins in the grid binning schemes. The shaded area shows the region of overlap between bins. The '1' and '0.5' labels indicate the weighting that is applied to the data, which varies linearly from 1 at the center of the bin to 0.5 at the edge of the bin.

Here we develop an approach to clearly image seismic discontinuities via deconvolution. We also incorporate an additional 4 years of data in comparison to Tharimena, Rychert, Harmon, et al. (2017). We focus on the SS precursor phases that reflect at the Moho (SmS) for validation purposes. We demonstrate the validity of our approach by applying it to synthetic seismograms. We also validate our approach by comparing the recovered global Moho depths with those from the Crust1.0 model (Laske et al., 2012). Finally, we discuss the potential of this method for imaging other discontinuities.

2. Methods

2.1 SS Data

We use the Incorporated Research Institutions for Seismology (IRIS) broadband dataset from 1990 to 2018, with event-to-station (epicentral) distances of 85° – 150°, for events with Mw > 5.5. Previous work has used a slightly more restricted range, e.g., 90° - 140° (Rychert & Shearer, 2010). However, this choice does not appear to strongly contaminate our resolution, as we will describe in the results and discussion section. We restricted our analysis to raw data from broadband channels (20 – 40 samples per second), and events with source depth < 75 km to minimize complications from depth phases. The seismic records are corrected to remove instrument responses and then rotated to radial and transverse components. We consider only the transverse components.

We convert all seismograms from displacement to acceleration, and then Hilbert transform them to produce symmetric SS pulses (Oppenheim & Schafer, 1975; Rychert & Shearer, 2010). The waveforms are resampled to 10 samples per second and band-pass filtered with corners at 0.02 Hz and 0.5 Hz. However, given the frequency content and dominant period of SS waves (~15 seconds), there is not much frequency content above this in the waveforms (Rychert & Shearer, 2011). An automated procedure is used to eliminate incomplete seismic records. We also use an automated procedure to center the waveforms on the SS phase, which is picked as the maximum positive or negative amplitude in a 10-second time window before and after the theoretical SS arrival time. The amplitude of the centered waveform is normalized to unit amplitude. We compute the signal-to-noise ratio (SNR) for each record as the ratio of the maximum amplitude of the seismic phase to the standard deviation in a time window 270 s to 30 s preceding the SS pulse. Visual inspection of a random sample of 2000 waveforms shows that the waveforms are generally poor quality for SNR < 3. Therefore, waveforms with SNR < 3 are rejected. In addition, seismic records with amplitude > 1 within a 90 s window preceding the normalized SS pulse are rejected. Finally, records with long-period noise evaluated as those with zero-crossings that occur at > 20 s intervals are also rejected. We obtain 4,962,579 seismic records that fit the source parameters described above, 1,648,704 of which also fit the signal-to-noise criteria. Our data provides improved spatial coverage over previous studies (Figure 2).

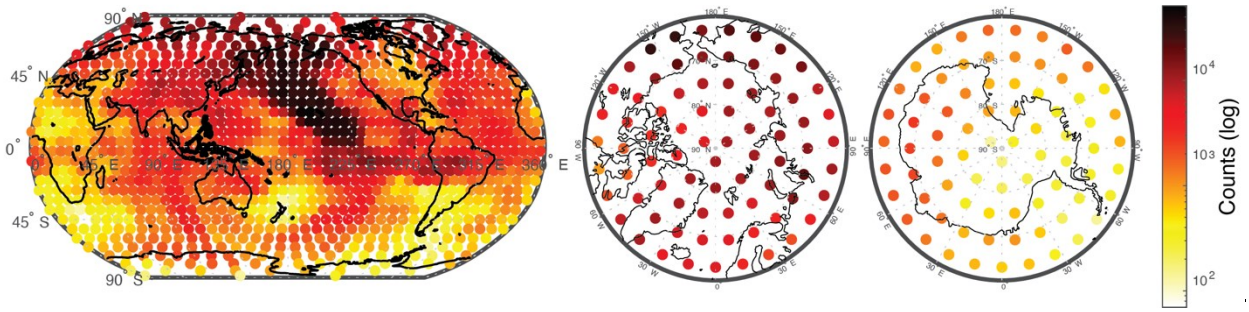

Figure 2: Maps showing the number of waveforms with SS phases and precursors in each bin that satisfy our requirements. Most of the Earth is shown (left) with the northern (central) and southern (right) hemisphere projections shown. 1,648,704 SS waveforms that satisfy our selection criteria are shown here.

2.2 Binning Schemes

Here we define a global binning scheme (Figure 2) for stacking waveforms. We divide the surface of the Earth into evenly distributed 6° circular bins with 30% overlap, resulting in 1146 bins.

SS precursors have saddle-shaped Fresnel zones (Tharimena et al., 2016). However, this effect can be mitigated by stacking waveforms along different azimuths, which results in a more circular region of sensitivity centered on our bins and the sensitivity region of the precursors (Figure 1). The large number of waveforms (>1000) and better azimuthal coverage in each bin compared to our previous work, minimizes the effect of off-axis structures in our study. In addition, we also linearly weight the waveforms depending on their distance from the bin center. We assign the highest weight of 1 to waveforms with bounce points closest to the bin center and a weight of 0.5 to waveforms with bounce points on the edges of the circular bin. This further ensures that the SS precursor stacks are more sensitive to the structure beneath the bounce points.

2.3 S Data and processing source wavelets

The SS phases are Hilbert transformed relative to the S phases (Choy & Richards, 1975). Therefore, the deconvolution of stacked source S phases from Hilbert transformed SS phases has the potential to separate the SS and SdS responses (Figure 3). We create event S-wave

source stacks that will be deconvolved from the SS waveforms (Rychert & Shearer, 2011; Tharimena, Rychert, & Harmon, 2017; Tharimena, Rychert, Harmon, et al., 2017; Tharimena et al., 2016). We follow similar processing steps described above for the SS. We use seismic records from 1990 – 2018, with epicentral distances of 25° – 80°, for events with magnitudes Mw > 5.5, and source depths < 75 km. We resample the data to 10 Hz and then apply a band-pass filter with corners at 0.02 Hz and 0.5 Hz. We use an automated approach to pick the seismic *S* phase as the maximum positive or negative amplitude pulse in a 10 s window before and after the theoretical S arrival time. The signal-to-noise ratio for each seismic record is calculated by comparing the maximum absolute value to the standard deviation in a time window 100 s – 20 s before the S phase. Waveforms with SNR < 2.8 are generally found to be of poor quality, with seismic coda before the S phase containing amplitudes as large as or greater than the S phase, and therefore they are rejected. The seismic records are then cut to a 40 s window centered on the picked S phase. The records are normalized to unit amplitude, and a 5 s cosine taper is applied to the ends of the wavelet. Finally, the source wavelets from all global receivers for a particular seismic event are stacked, scaling by individual SNRs to produce source stacks. We obtain 11,484 unique source stacks, for the events from 1990 – 2018 in our study.

2.4 Deconvolution, Migration and Stacking *SS* Waveforms

We deconvolve the S wavelet stack of the corresponding event from each SS waveform using an extended time multi-taper frequency domain deconvolution method (Helffrich, 2006; Rychert et al., 2012) (Figure 3). The deconvolution method is a hybrid between multi-taper deconvolution and Welch's method for spectra estimation. Specifically, the method sums multi-taper cross and auto spectral estimates on several overlapping windows across the records and then performs the deconvolution. We use a 30 s window, with a 50% overlap on each window, a time-bandwidth product of 3 that translates to a frequency bandwidth of permissible spectral leakage of 0.2 Hz and 4 tapers (Shibutani et al., 2008). This results in an impulse response function that corresponds to the discontinuity structure beneath the bounce point. Deconvolutions of individual waveforms are normalized to the SS phase amplitude. The

normalized impulse response functions with amplitudes larger than 1 in precursor sections are rejected.

The impulse response functions are then migrated to depth, stacked, and Moho depths are estimated. For the crust, we use a smoothed version of Crust1.0, corresponding to the average thickness and velocity within the 6° bin. For the mantle we use the IASP91 model, beginning at sub-crustal depths. Finally, we stack the migrated impulse response functions scaled according to their signal-to-noise ratio and distance from the bin center (section 2.2). We then search automatically for the peak in the stack arriving before the main SS pulse, which is likely related to the Moho discontinuity.

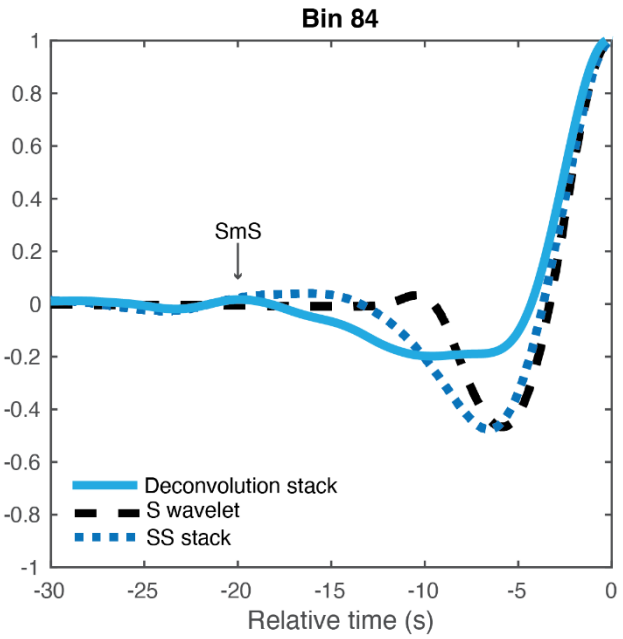

Figure 3: Deconvolutions of real data. Stacked S wavelet of an earthquake of Mw 6.9 that occurred at 06:48:10, Feb. 19, 1990, at west of Luganville, Vanuatu, which contributes 30 waveforms to Bin 84, and all SS waveforms and deconvolutions stacked from Bin 84, located in North America. SmS phases are indicated by arrows.

2.5 Validation

We validate our approach by applying it to synthetic seismogram data calculated using the spectral element solver AxiSEM (Nissen-Meyer et al., 2014) which creates full waveform

synthetics assuming a spherically symmetric Earth model. AxiSEM separates the problem of wave propagation in a symmetric medium into an analytical solution of the problem in the azimuthal (ϕ) direction perpendicular to the source-receiver plane and a numerical spectral-element discretization within the in-plane r, θ, which reduces the numerical cost to that of about a 2D method (Nissen‐Meyer et al., 2007) and includes attenuation and anisotropy. We used a source with the following focal mechanism parameters: M0=$1e^{21}$, strike=32, dip=62. We then generate wavefields for the 1-D velocity models modified from the reference earth model PREM (Dziewonski & Anderson, 1981) including a velocity increase at a range of potential Moho depths: 10, 20, 30, 40 and 60 km and one without crust. For models with Moho depths at 10 and 20 km, we replace the upper crust layer (≤ 15 km) in the PREM model with lower crust parameters and set the Moho at corresponding depths. For other models with deeper Mohos we extend the deeper crustal layer to the corresponding Moho depths. We process the synthetics in the same way we process the data and use the input model to translate the resulting receiver functions to depth.

Instaseis (van Driel et al., 2015), a python package, is used to reconstruct seismograms for a source defined by moment-tensor and receiver locations using the precalculated wavefield databases. This is possible due to the reciprocity of the Green's function which permits switching the location of source and receiver of a seismic wavefield. *Instaseis* uses the stored displacement wavefield to calculate strain, which enables simulation of arbitrary moment tensors and source time functions.

We also compare the depth of SmS phase in each data bin to Crust1.0. The standard deviation of error between resolved crust thickness and Crust1.0 is 4 km, which is the value we report as the error here.

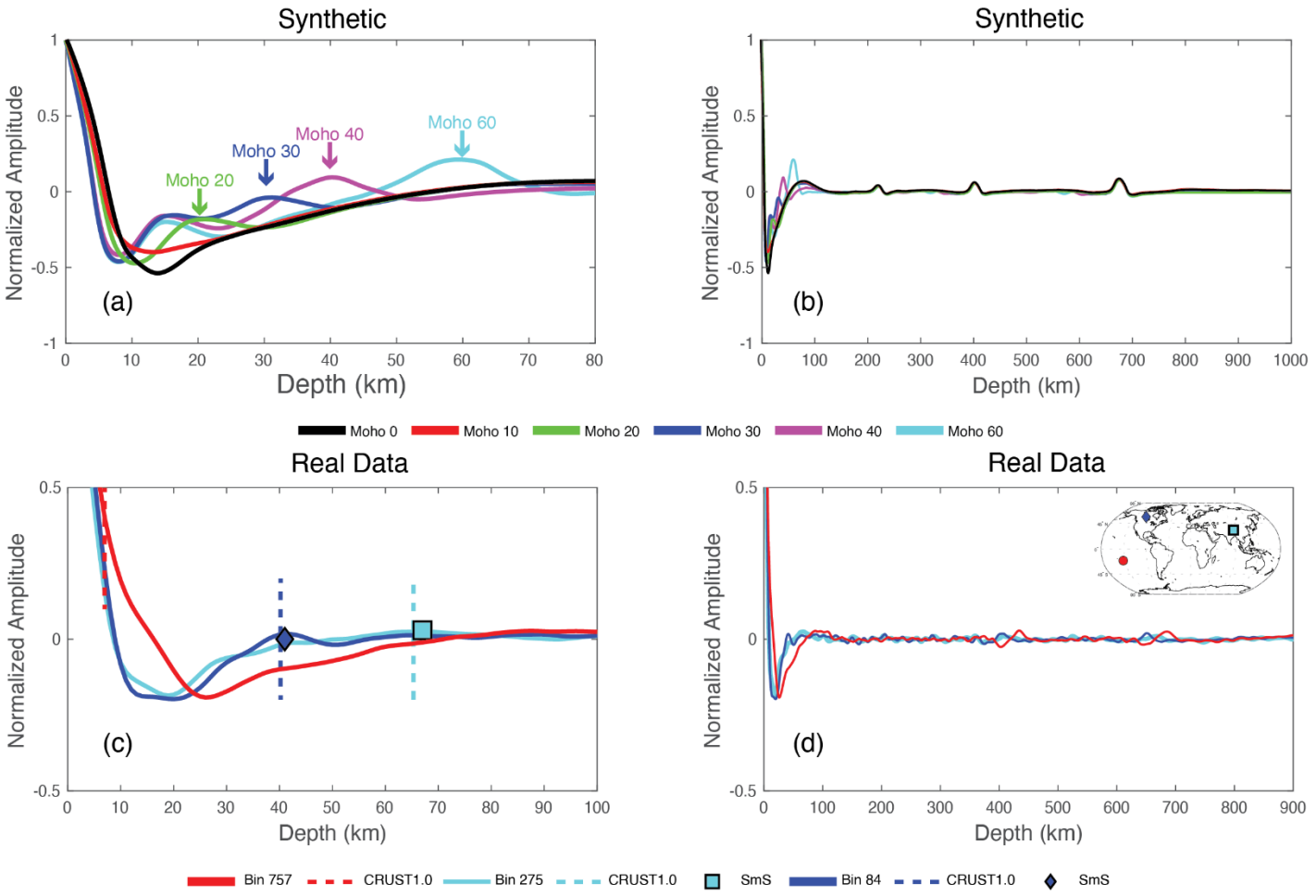

Figure 4: Synthetic and real examples. (a) SS synthetics were calculated for models modified from PREM to incorporate a Moho at 10, 20, 30, 40, and 60 km depth and a model without a Moho. The synthetics were processed in the same way we process the data. We calculated waveforms from a range of epicentral distances (each degree from 85° - 150°) and stacked the resulting waveforms on the SS phase and migrated to depth. The resolved corresponding Moho depths are marked by arrows. (b) Same as (a) but in a longer depth window. (c) Examples of real data in Bin 84, 757, and 275. Bin 757 represents an oceanic region where we failed to resolve the Moho. Bin 84 represents normal crust in North America and bin 275 represents a bin with thick crust in Tibet, which we resolve (diamond and square) in comparison to Crust1.0 (dashed line). (d) Same as (c) but in a longer depth window. Markers in the inset map show the locations of these three bins, blue diamond for Bin 84, cyan square for Bin 275, and red circle for Bin 757.

3. Results and Discussion

The resolution testing with synthetics shows that we can resolve discontinuities as shallow as 20 km depth (Figure 4). We also resolve phases at 15 km depth for the synthetic models with Mohos at ≥ 30 km, since this discontinuity exists in the PREM model (Figure 4a). However, it does not impact the resolution of the deeper Moho depths.

For real data, regions with Moho depths < 20 km are not well-resolved. Therefore, we focus only on discontinuities at ≥ 20 km depth. This includes 397 bins out of 415 bins with continental crust according to the 3SMAC (Nataf & Ricard, 1996) classification.

Our SS precursor method applied to the data resolves the Moho globally beneath the continents well. We image a Moho at 21 – 67 km depth beneath the continents. The thickest crust, 67 ± 4 km depth, is imaged beneath the Himalayan region of Asia.

Our results are in excellent agreement with crustal thickness from Crust1.0 averaged over our bins in continental regions (Laske et al., 2012) (Figure 5). Our result is a minimum of 9 km shallower than Crust1.0 in all locations (Figure 6). Our result is deeper than 10 km than Crust1.0 in 19 % of bins with Crust > 20 km. The outliers are all located in coastal areas except for 1 bin in Africa. The reason for this asymmetry and the fact that SS cannot resolve the coastal bins is because the depths of the Crust1.0 model averaged over the bin areas are relatively shallow, given nearby oceanic crust. However, shallow, oceanic Moho phases fall within the main SS pulse and do not affect its sidelobe or resulting Moho depth (Rychert & Shearer, 2010). Therefore, the only resolved SS Moho in these coastal regions is from the thicker continental regions. In addition, thick sediments near coastal regions could add greater complexity (Wang et al., 2022). Excluding the 76 outlier coastal bins, observed crust thicknesses of the remaining 321 bins are correlated with Crust1.0 model at 0.81, and 70 % of those bins are resolved within 5 km of Crust1.0, with a correlation coefficient of 0.93. This verifies that this method can be used to resolve discontinuities, although we do not believe that it supersedes Crust1.0.

Overall, the increase in data quantity and improved method demonstrates enhanced resolution capabilities in comparison to previous work (Rychert & Shearer, 2010) . Rychert and Shearer (2010) resolved the Moho in 30 10° bins beneath Asia and at depths > 25 km, a region of particularly large bounce point coverage and deep Moho depths and found Moho depths correlated with Crust2.0 at 0.82. However, we resolve the Moho beneath 321 bins in

continental regions at depths as shallow as 20 km. Negative phases at sub-Moho depths may cause artificial LAB phases and/or interfere with LAB phases. Therefore, future work is required to assess the viability of this approach for the LAB; however, this method will be useful for other deeper discontinuities such as those of the mantle transition zone. From synthetic testing, despite variations of crust thickness, the discontinuities at 200 km, 400 km and 670 km in the PREM models were well resolved. Moreover, we also find clear phases associated with the mantle transition zone in real data even though the parameters, e.g. epicenter distances, and bandpass, used in this work may not be ideal to image them (Figure 4).

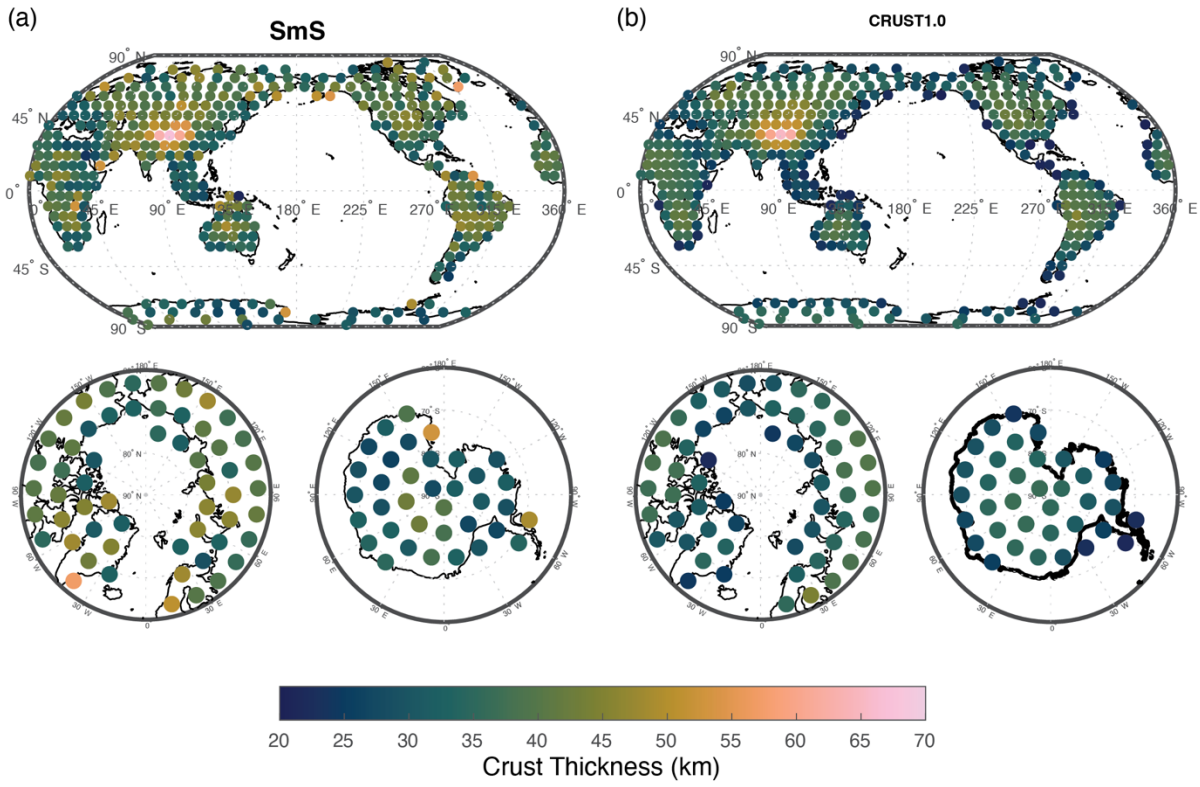

Figure 5. Crust thickness. (a) Crust thickness measured from SmS phases. Top: global view; Bottom left: Antarctic view; Bottom right: Arctic view. (b) Same as (a), Crust thickness from Crust1.0 model.

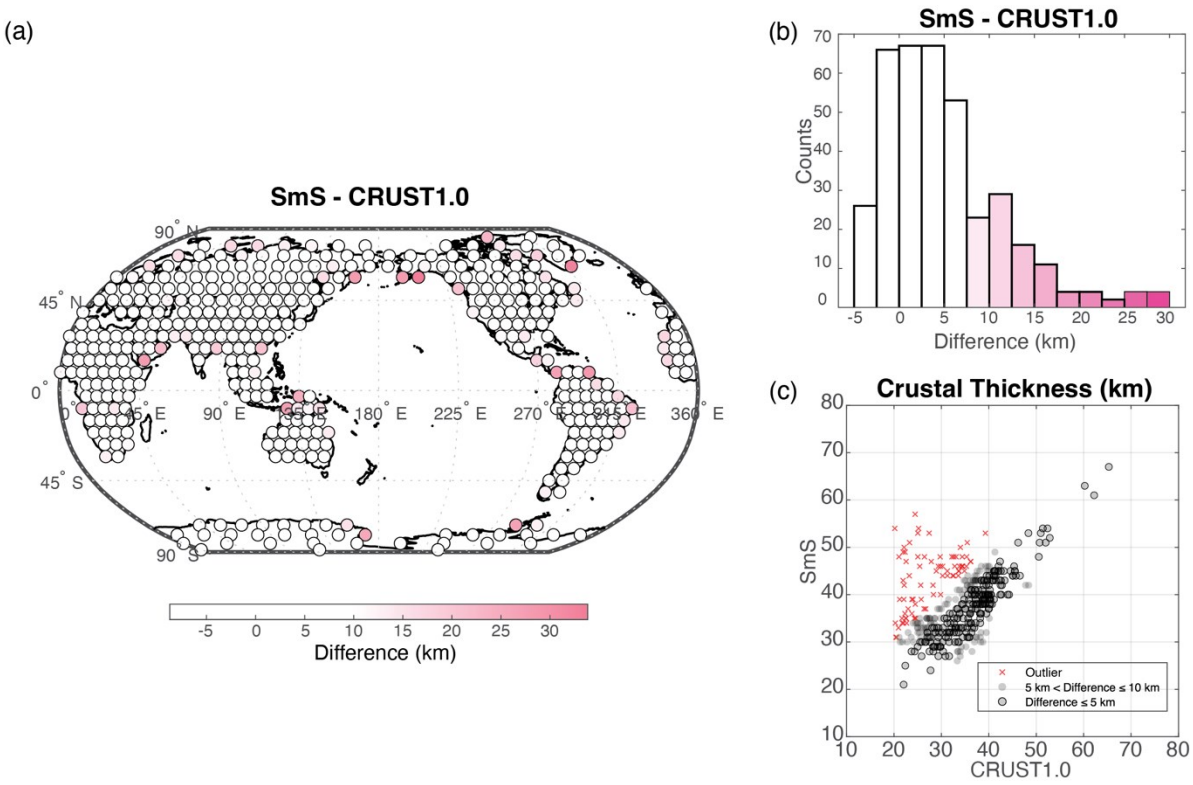

Figure 6: Comparisons to Crust1.0. (a) Differences between Crustal thickness from SS precursors, SmS phases, and Crust1.0 model. (b) Histogram of different crustal thicknesses between SmS and the Crust1.0 model. (c) Comparisons of Crustal thickness from SmS phases, and the Crust1.0 model. Semi-transparent dots show cases with differences of 5 - 10 km from Crust1.0. Semi-transparent dots with outlines show cases with differences of ≤ 5 km from Crust1.0. Red crosses show data with differences larger than 10 km, shown as pink dots in (a), which are primarily in coastal regions.

4. Conclusion

We developed a new SS precursor imaging method that achieves high-resolution imaging, 6° X 6°, of discontinuities as shallow as 20 km depth. We verified that the method resolves structures as shallow as 20 km depth by applying it to AxiSEM synthetics calculated for a PREM model modified to include velocity increases at potential Moho depths between 10 and 60 km depth. We also validated the method by comparing the Moho resolved by data stacked in 6° bins to Crust1.0. We find that we can resolve Moho depths ≥ 20 km from Crust1.0 within the continental interior in all cases, and in 77 % of all continental regions, with outliers in

coastal regions. Both synthetic and data examples demonstrate mantle transition zone discontinuities are also well resolved. Overall, this approach shows much promise for imaging discontinuity structure of other discontinuities at high resolution in the future.

5. Acknowledgement

This work is supported in part by Natural Environment Research Council, UK grants NE/M003507/1 (PI-LAB) and the European Research Council (GA 638665) (EURO-LAB). The authors acknowledge the use of the IRIDIS High Performance Computing Facility, and associated support services at the University of Southampton in the completion of this work.

6. Data and Code Availability

Global data used for this study is available from the Incorporated Research Institutions for Seismology (IRIS) Data Management Center (DMC) website https://ds.iris.edu/ds/nodes/dmc. AxiSEM/Instaseis database of PREM is available at IRIS DMC. A version of the code used in this work is available upon request.

7. References

Artemieva, I. (2011). *The Lithosphere: An Interdisciplinary Approach*. Cambridge University Press. https://doi.org/DOI: 10.1017/CBO9780511975417

Bassin, C., Laske, G., & Masters, G. (2000). The current limits of resolution for surface wave tomography in North America. *EOS Transactions, Fall Meeting Suppliment, AGU*, *81*(F897).

Bostock, M. G. (1999). Seismic imaging of lithospheric discontinuities and continental evolution. *Lithos*, *48*(1-4), 1-16. <Go to ISI>://000083177600002

Choy, G. L., & Richards, P. G. (1975). Pulse distortion and Hilbert transformation in multiply reflected and refracted body waves. *Bulletin of the Seismological Society of America*, *65*(1), 55-70. https://doi.org/10.1785/bssa0650010055

Dziewonski, A. M., & Anderson, D. L. (1981). Preliminary Reference Earth Model. *Physics of the Earth and Planetary Interiors*, *25*(4), 297-356. <Go to ISI>://A1981LV59500002

Eaton, D. W., Darbyshire, F., Evans, R. L., Grutter, H., Jones, A. G., & Yuan, X. H. (2009). The elusive lithosphere-asthenosphere boundary (LAB) beneath cratons. *Lithos*, *109*(1-2), 1-22. https://doi.org/10.1016/j.lithos.2008.05.009

Fischer, K. M., Ford, H. A., Abt, D. L., & Rychert, C. A. (2010). The Lithosphere-Asthenosphere Boundary. *Annual Review of Earth and Planetary Sciences*, *38*(1), 551-575. https://doi.org/Doi 10.1146/Annurev-Earth-040809-152438

Flanagan, M. P., & Shearer, P. M. (1998). Global mapping of topography on transition zone velocity discontinuities by stacking SS precursors. *Journal of Geophysical Research: Solid Earth*, *103*(B2), 2673-2692. https://doi.org/https://doi.org/10.1029/97JB03212

Frazer, W. D., & Park, J. (2023). High-resolution mid-mantle imaging with multiple-taper SS-precursor estimates. *Geophysical Journal International*, *233*(2), 1356-1371. https://doi.org/10.1093/gji/ggac491

Harmon, N., Forsyth, D. W., & Weeraratne, D. S. (2009). Thickening of young Pacific lithosphere from high-resolution Rayleigh wave tomography: A test of the conductive cooling model. *Earth and Planetary Science Letters*, *278*(1-2), 96-106. https://doi.org/10.1016/j.epsl.2008.11.025

Heit, B., Yuan, X. H., Bianchi, M., Kind, R., & Gossler, J. (2010). Study of the lithospheric and upper-mantle discontinuities beneath eastern Asia by SS precursors. *Geophysical Journal International*, *183*(1), 252-266. <Go to ISI>://WOS:000281902600019

Helffrich, G. (2006). Extended-time multitaper frequency domain cross-correlation receiver-function estimation. *Bulletin of the Seismological Society of America*, *96*(1), 344-347. https://doi.org/10.1785/0120050098

Houser, C., Masters, G., Flanagan, M., & Shearer, P. (2008). Determination and analysis of long-wavelength transition zone structure using SS precursors. *Geophysical Journal International*, *174*(1), 178-194. https://doi.org/10.1111/j.1365-246X.2008.03719.x

Huang, Q., Schmerr, N., Waszek, L., & Beghein, C. (2019). Constraints on Seismic Anisotropy in the Mantle Transition Zone From Long-Period SS Precursors. *Journal of Geophysical Research: Solid Earth*, *124*(7), 6779-6800. https://doi.org/https://doi.org/10.1029/2019JB017307

Laske, G., Masters, G., Ma, Z., & Pasyanos, M. (2012). CRUST1.0: An updated global model of Earth's crust. *Geophysical Research Abstracts*.

Masters, G., Johnson, S., Laske, G., & Bolton, H. (1996). A shear-velocity model of the mantle. *Philosophical Transactions of the Royal Society a-Mathematical Physical and Engineering Sciences*, *354*(1711), 1385-1410. https://doi.org/DOI 10.1098/rsta.1996.0054

Mehouachi, F., & Singh, S. C. (2018). Water-rich sublithospheric melt channel in the equatorial Atlantic Ocean. *Nature Geoscience*, *11*(1), 65-69. https://doi.org/10.1038/s41561-017-0034-z

Meier, U., Curtis, A., & Trampert, J. (2007). Global crustal thickness from neural network inversion of surface wave data. *Geophysical Journal International*, *169*(2), 706-722. https://doi.org/10.1111/j.1365-246X.2007.03373.x

Mohorovičić, A. (1910). Potres od 8. X. 1909. *Godišnje izvješće zagrebačkog meteorološkog opservatorija za godinu 1909*.

Montagner, J. P., & Tanimoto, T. (1991). Global upper mantle tomography of seismic velocities and anisotropies. *Journal of Geophysical Research*, *96*, 15.

Nataf, H. C., & Ricard, Y. (1996). 3SMAC: An a priori tomographic model of the upper mantle based on geophysical modeling. *Physics of the Earth and Planetary Interiors*, *95*(1-2), 101-122. https://doi.org/Doi 10.1016/0031-9201(95)03105-7

Nissen-Meyer, T., van Driel, M., Stähler, S. C., Hosseini, K., Hempel, S., Auer, L., Colombi, A., & Fournier, A. (2014). AxiSEM: broadband 3-D seismic wavefields in axisymmetric media. *Solid Earth*, *5*(1), 425-445. https://doi.org/10.5194/se-5-425-2014

Nissen‐Meyer, T., Fournier, A., & Dahlen, F. A. (2007). A two‐dimensional spectral‐element method for computing spherical‐earth seismograms – I. Moment‐tensor source. *Geophysical Journal International*, *168*(3), 1067-1092. https://doi.org/10.1111/j.1365-246X.2006.03121.x

Oppenheim, A. V., & Schafer, R. W. (1975). *Digital Signal Processing*. Prentice-Hall, Inc.

Price, K. V., Storn, R. M., & Lampinen, J. A. (2005). *Differential Evolution: A Practical Approach to Global Optimization* Springer.

Ringwood, A. E. (1975). *Composition and Petrology of the Earth's Mantle*. McGraw-Hill. https://www.cambridge.org/core/article/a-e-ringwood-composition-and-petrology-of-the-earths-mantle-london-new-york-and-sydney-mcgrawhill-1975-xviii618-pp-153-figs-price-1945/CCF1A77CC01E1C6581008EA19FEEC877

Ritsema, J., Deuss, A., van Heijst, H. J., & Woodhouse, J. H. (2011). S40RTS: a degree-40 shear-velocity model for the mantle from new Rayleigh wave dispersion, teleseismic traveltime and normal-mode splitting function measurements. *Geophys. J. Int.*, *184*(3), 1223-1236. https://doi.org/10.1111/j.1365-246X.2010.04884.x

Roy Chowdhury, K. (2020). Deep Seismic Reflection and Refraction Profiling. In H. K. Gupta (Ed.), *Encyclopedia of Solid Earth Geophysics* (pp. 1-18). Springer International Publishing. https://doi.org/10.1007/978-3-030-10475-7_226-1

Rychert, C. A., Fischer, K. M., & Rondenay, S. (2005). A sharp lithosphere-asthenosphere boundary imaged beneath eastern North America. *Nature*, *436*(7050), 542-545. <Go to ISI>://000230788800058

Rychert, C. A., Harmon, N., Constable, S., & Wang, S. (2020). The Nature of the Lithosphere-Asthenosphere Boundary. *Journal of Geophysical Research: Solid Earth*, *125*(10), e2018JB016463. https://doi.org/10.1029/2018jb016463

Rychert, C. A., Harmon, N., & Tharimena, S. (2018). Seismic Imaging of the Base of the Ocean Plates. *Lithospheric Discontinuities*, 71-87. https://doi.org/doi:10.1002/9781119249740.ch4

10.1002/9781119249740.ch4 (Geophysical Monograph Series)

Rychert, C. A., Rondenay, S., & Fischer, K. M. (2007). P-to-S and S-to-P imaging of a sharp lithosphere-asthenosphere boundary beneath eastern North America. *Journal of Geophysical Research-Solid Earth*, *112*(B8). https://doi.org/Artn B08314

10.1029/2006jb004619

Rychert, C. A., Schmerr, N., & Harmon, N. (2012). The Pacific lithosphere-asthenosphere boundary: Seismic imaging and anisotropic constraints from SS waveforms. *Geochemistry Geophysics Geosystems*, *13*. https://doi.org/Artn Q0ak10

10.1029/2012gc004194

Rychert, C. A., & Shearer, P. M. (2009). A Global View of the Lithosphere-Asthenosphere Boundary. *Science*, *324*(5926), 495-498. https://doi.org/10.1126/science.1169754

Rychert, C. A., & Shearer, P. M. (2010). Resolving crustal thickness using SS waveform stacks. *Geophys. J. Int.*, *180*(3), 1128-1137. https://doi.org/10.1111/j.1365-246X.2009.04497.x (10.1111/J.1365-246x.2009.04497.X)

Rychert, C. A., & Shearer, P. M. (2011). Imaging the lithosphere-asthenosphere boundary beneath the Pacific using SS waveform modeling. *Journal of Geophysical Research-Solid Earth*, *116*. <Go to ISI>://WOS:000293345400003

Rychert, C. A., Shearer, P. M., & Fischer, K. M. (2010). Scattered wave imaging of the lithosphere–asthenosphere boundary. *Lithos*, *120*(1-2), 173-185. https://doi.org/DOI 10.1016/j.lithos.2009.12.006

Schmerr, N. (2012). The Gutenberg Discontinuity: Melt at the Lithosphere-Asthenosphere Boundary. *Science*, *335*(6075), 1480-1483. https://doi.org/10.1126/science.1215433

Shearer, P. M. (1991). Constraints on Upper Mantle Discontinuities from Observations of Long-Period Reflected and Converted Phases. *Journal of Geophysical Research-Solid Earth*, *96*(B11), 18147-18182. https://doi.org/Doi 10.1029/91jb01592

Shibutani, T., Ueno, T., & Hirahara, K. (2008). Improvement in the extended-time multitaper receiver function estimation technique. *Bulletin of the Seismological Society of America*, *98*(2), 812-816. https://doi.org/10.1785/0120070226

Stern, T. A., Henrys, S. A., Okaya, D., Louie, J. N., Savage, M. K., Lamb, S., Sato, H., Sutherland, R., & Iwasaki, T. (2015). A seismic reflection image for the base of a tectonic plate. *Nature*, *518*(7537), 85-88. https://doi.org/10.1038/nature14146

Storn, R., & Price, K. (1997). Differential evolution - A simple and efficient heuristic for global optimization over continuous spaces. *Journal of Global Optimization*, *11*(4), 341-359. https://doi.org/Doi 10.1023/A:1008202821328

Tharimena, S., Rychert, C., & Harmon, N. (2017). A unified continental thickness from seismology and diamonds suggests a melt-defined plate. *Science*, *357*(6351), 580-583.

Tharimena, S., Rychert, C., Harmon, N., & White, P. (2017). Imaging Pacific lithosphere seismic discontinuities—Insights from SS precursor modeling. *Journal of Geophysical Research: Solid Earth*, *122*(3), 2131-2152.

Tharimena, S., Rychert, C. A., & Harmon, N. (2016). Seismic imaging of a mid-lithospheric discontinuity beneath Ontong Java Plateau. *Earth and Planetary Science Letters*, *450*, 62-70.

van Driel, M., Krischer, L., Stähler, S. C., Hosseini, K., & Nissen-Meyer, T. (2015). Instaseis: instant global seismograms based on a broadband waveform database. *Solid Earth*, *6*(2), 701-717. https://doi.org/10.5194/se-6-701-2015

Wang, P., Zhou, Y., Xu, M., Zhang, H., Chen, X., & Guo, L. (2022). Investigation of Effects of Near‐Surface Complexities on Measurement of Mantle Discontinuity Using SS and Its Precursors. *Journal of Geophysical Research: Solid Earth*, *127*(9), e2022JB024485.